Article:
Li, W., Li, H., Chen, X. et al. (2025) Data-driven open-circuit fault diagnosis for PMSM drives: feature extraction via normalized current space vector sorting. IEEE Transactions on Industry Applications. pp. 1-11. ISSN: 0093-9994

https://doi.org/10.1109/tia.2025.3644988

Data-Driven Open-Circuit Fault Diagnosis for PMSM Drives: Feature Extraction via Normalized Current Space Vector Sorting

Weiqian Li, *Student Member, IEEE*, Huanyu Li, *Student Member, IEEE*, Xiao Chen, *Senior Member, IEEE*, Antonio Griffo, and Xiangyu Sun, *Student Member, IEEE*

***Abstract*—Open-circuit faults in three-phase voltage source inverters can cause unbalanced currents, high torque ripple, and excessive core losses in permanent magnet synchronous machines. To effectively diagnose these faults, a novel fault feature extraction method based on normalized current space vector sorting is proposed. This approach transforms the three-phase currents under different fault conditions into unique fault patterns, ensuring a clear distinction between fault modes. Moreover, this method is robust to variations in torque and speed, ensuring reliable diagnosis across diverse operating conditions. To enhance fault detection capabilities, a one-dimensional convolutional neural network (1D-CNN) is designed to capture both local and global features effectively. The model is initially pre-trained using simulated data, with data augmentation applied to improve robustness and facilitate the learning of domain-invariant features. Simulation and experimental results validate the superiority of the proposed method over existing open-circuit fault diagnosis techniques across multiple evaluation metrics. Additionally, the proposed method's simple network architecture, fast inference times, high diagnostic accuracy and strong robustness make it a practical and efficient solution for real-world fault diagnosis applications.**

Keywords—open-circuit faults, machine learning, current sorting, PMSM, voltage source inverter, 1DCNN

I. Introduction

Voltage source inverters (VSIs) are widely used in permanent magnet synchronous motor (PMSM) due to their efficient performance. In industrial, the reliability of VSIs is a critical concern, particularly due to the susceptibility of power devices such as insulated gate bipolar transistors (IGBTs) to faults [2]. These faults are primarily categorized into short-circuit (SC) and open-circuit (OC) faults. SC faults typically result in overcurrent and immediate system shutdown through protection mechanisms, whereas OC faults, which do not usually trigger protection systems, can degrade system performance over time and cause secondary damages, such as torque fluctuations and motor overheating [3]. As the complexity of power systems increases, effective fault diagnosis, particularly for OC faults, is essential to ensure the reliability and safety of energy conversion systems.

Fault diagnosis methods for OC faults in inverters can be broadly categorized into model-based, signal-based, and Artificial Intelligence (AI)-based methods. Model-based methods involve creating mathematical models of the system and comparing predicted outputs with actual measurements to detect discrepancies. Examples include model reference adaptive system (MRAS) schemes for PWM VSIs [4], observer-based diagnostics with adaptive thresholds in PMSM drives [5], voltage-envelope residuals for single-switch OC localization [6], Model predictive control (MPC) residual analysis [7], hybrid logic dynamic models for residual-vector estimation [8], and sensorless switching-function detectors achieving sub-cycle response [9]. Although these methods are effective, they typically rely on accurate mathematical models, which can be challenging to develop for complex systems. Signal-based approaches extract features directly from measured currents or voltages. Techniques include seasonal-trend decomposition [10]. Discrete Fourier transform (DFT) and Principal component analysis (PCA) for feature extraction and dimensionality reduction [11] [12]. Another method identified faults using low-cost, fast time-domain analysis with rotatory reference systems and basic arithmetic operations [13]. A double normalization strategy normalizing both current amplitude and phase to ensure robust OC fault detection under varying torque and speed conditions [14]. The method in [15] detects single and double SC faults in three-phase current source converters by analyzing output current vector amplitude and phase. Whereas signal processing can be effective, it often brings a relatively heavy computational burden and excessive diagnostic time, requiring expert knowledge.

With the advancement of machine learning (ML), AI-based fault diagnosis methods have increasingly become a research focus [16] [17]. Classical ML methods such as support vector machines (SVM), k-nearest neighbour (KNN), random forests (RF), multi-layer perceptron (MLP), have been explored [17-21]. For example, the current trajectory slope was used as the fault feature in conjunction with the RF as fault classiffer [18], echoing the effectiveness of other RF-based methods in handling nonstationary conditions [19]. To adapt a trained diagnostic model in different systems, another study transformed features through manifold learning [20], while deep belief networks (DBNs) combined with least square support vector machines (LSSVMs) optimize feature selection in rectifiers under distortion [21] and pyramid-shaped nets extract high-dimensional feature vectors [22].

Additionally, CNN has been widely used in fault pattern recognition tasks due to their powerful feature extraction capabilities [23]. For instance, 1D CNNs for modular multilevel converter OC faults deliver 99.77 % accuracy in 80 ms [24], CNNs classify 18 OC types in hybrid active neutral-point

clamped (HANPC) inverters under varying load currents [25], an enhanced stochastic-gradient 1D-CNNs enable fast NPC fault diagnosis [26], and edge-optimized CNN lightweight networks run three times faster in 3L-ANPC diagnosis with TensorRT [27]. Nonetheless, these CNN-based methods typically require large amounts of training data. A wavelet 2D-CNN hybrids maintain accuracy with fewer samples, but the 2D input and wavelet adds to the computational complexity [28].

The paper proposes a novel fault feature extraction method for open-circuit fault diagnosis in VSI. This paper is an extension of [1]. The extracted fault patterns effectively distinguish different fault types and demonstrate strong robustness under various operating conditions. The proposed feature extraction method converts three-phase currents into a dual-channel sequence, making it compatible with various machine learning models, particularly 1D-CNN-based classification models. This enables high diagnostic accuracy even with a simple network structure. Compared to existing data-driven approaches [18] [20] [22] [29], the proposed method relies solely on simulation data for offline training, significantly reducing data acquisition costs. Additionally, data augmentation techniques further enhance the model generalization ability and robustness.

The remainder of this article is organized as follows: Section II provides a detailed description of the proposed method, Section III introduces the simulation verification, while experimental verification and comparative analysis are conducted in Section IV, and Section V draws conclusion.

In addition, the contributions of this article are described as follows.

1) Feature extraction: An angle-sorted normalized current space-vector is introduced: three-phase currents are Clarke-transformed, amplitude-normalized, and sorted by instantaneous electrical angle, yielding a locally steady two-channel sequence that suppresses fault-irrelevant segments and exposes OC-specific distortions, robust to condition variation.
2) Diagnosis pipeline and validation: A lightweight 1D-CNN matched to this representation is employed with simulation-only pretraining and noise augmentation for cross-domain robustness; online validation establishes real-time feasibility and rapid localization.

II. OC Fault Diagnosis Method

The topology of the voltage source inverter is illustrated in Fig. 1, and the fault modes are categorized into healthy, one switch OC, and two-switch OC, with all operating states presented in Table I.

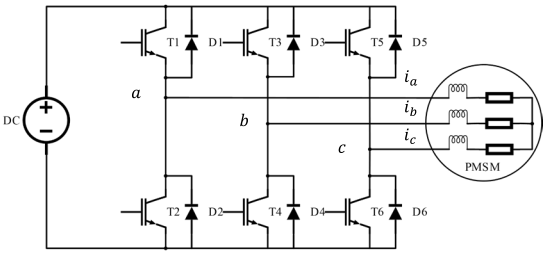

Fig. 1. Topology of three-phase inverter.

TABLE I
OC Fault Modes of Inverter

Operation states	Open circuit switches
Healthy	None
One switch OC	T1, T2, T3, T4, T5, T6
Two switch OC	T12, T13, T14, T15, T16, T23, T24, T25, T26, T34, T35, T36. T45, T46,T56

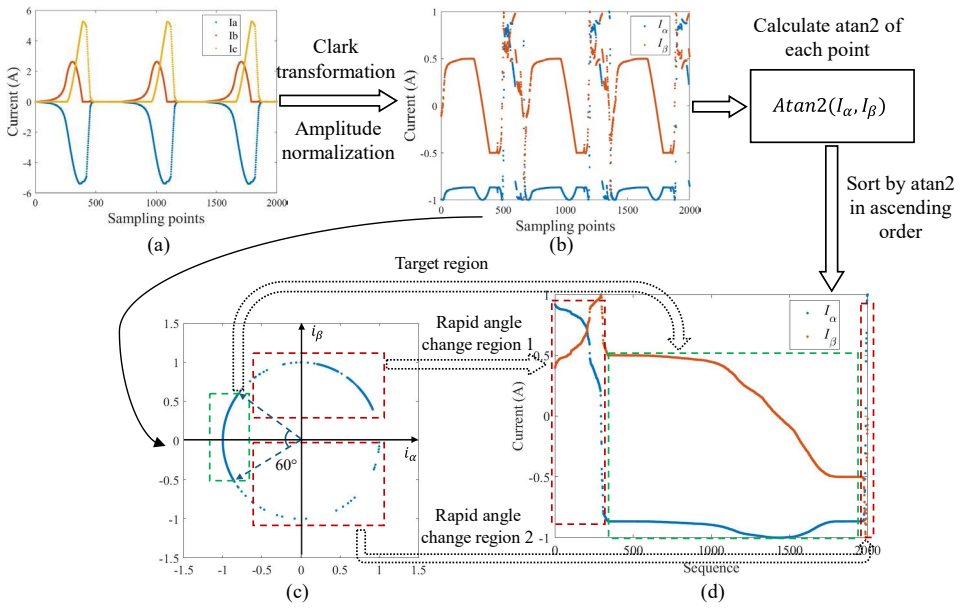

Fig. 2. Procedures of proposed fault diagnosis method, with PMSM operating at 500r/min, 2.5Nm, two switches T46 OC. (a) Three phase currents of PMSM. (b) Normalized currents in two-phase coordinate system. (c) Normalized current vector trajectory in which rapid angle change regions do not cross the positive *x*-axis. (d) Sorted normalized current vector.

To extract the fault features, the procedures are described as follows.

Step 1: Converting the three-phase currents sampled at a given frequency into the two-phase $\alpha\beta$ coordinate system via Clarke transformation through (1) and (2).

$$\begin{cases} i_a = I_m \cos\theta \\ i_b = I_m \cos(\theta - 2\pi/3) \\ i_c = I_m \cos(\theta + 2\pi/3) \end{cases} \tag{1}$$

$$\begin{bmatrix} i_\alpha \\ i_\beta \end{bmatrix} = \frac{2}{3}\begin{bmatrix} 1 & -\frac{1}{2} & -\frac{1}{2} \\ 0 & \frac{\sqrt{3}}{2} & -\frac{\sqrt{3}}{2} \end{bmatrix}\begin{bmatrix} i_a \\ i_b \\ i_c \end{bmatrix} \tag{2}$$

where i_α and i_β are $\alpha\beta$-axes currents, I_m is the amplitude of phase current, and the process is depicted in Fig. 2(a).

Step 2: Calculating the amplitude of the current vector using i_α and i_β, and normalizing the currents through (3).

$$|I_s| = \sqrt{i_\alpha^2 + i_\beta^2}$$
$$I_{sv} = \frac{I_s}{|I_s|} = \sin\theta + j\cos\theta = \angle\theta_s \tag{3}$$

where I_s is the current vector, and I_{sv} is the normalized current space vector. The waveform of I_{sv} is shown in Fig. 2(b).

Step 3: Calculating the 2-argument arctangent $atan2(y,x)$ (in radians, $(-\pi,\ \pi]$), which is the angle between the positive x-axis and the normalised current vector $(\frac{i_\alpha}{|I_s|}, \frac{i_\beta}{|I_s|})$,) in the Cartesian plane, and then adjust the $atan2(y,x)$ range to $(0, 2\pi]$ through (4).

$$atan2(y,x) = atan2(y,x) + 2\pi \quad \text{if } atan2(y,x) < 0 \tag{4}$$

Since the adjusted $atan2(y,x)$ increases monotonically when $atan2(y,x) \in [0, 2\pi]$, sort each point (i_α, i_β) in ascending order based on the corresponding $atan2$ value, and finally obtain the sorted normalized current as the fault patterns.

Step 4: A 2-channel 1D-CNN is designed to recognize the fault patterns, before fault and healthy samples are collected by running the Simulink model in multiple setting operating states. The samples are split into training set and test set, as input to the 1D-CNN for evaluation.

To further illustrate the role of current sorting, the normalized current space vector is plotted in the $\alpha\beta$ coordinate system, with its trajectories dispersed along a circle with a radius of 1, as shown in Fig. 2(c). The trajectory is segmented into two regions: rapid angle change and target. Due to the OC fault conditions, there are regions where the amplitude of the current vector is close to zero; therefore, the angle of the normalised current vector changes very quickly. We define these regions as 'rapid angle change', which are considered irrelevant fault feature and are marked by red dashed boxes. These regions occur when the current space-vector amplitude $|I_s|$ is small, which makes the feature angle $\theta_s = atan2(i_\alpha, i_\beta)$ highly sensitive to perturbations. The local sensitivities are included as

$$\frac{\partial\theta_s}{\partial i_\alpha} = -\frac{i_\beta}{i_\alpha^2 + i_\beta^2}, \qquad \frac{\partial\theta_s}{\partial i_\beta} = \frac{i_\alpha}{i_\alpha^2 + i_\beta^2}, \tag{5}$$

and note that $\|\nabla\theta_s\| = \frac{1}{|I_s|}$, hence θ_s is ill-conditioned as $|I_s|$ close to 0. Therefore, these regions are excluded to reduce within-class variance and improve classification reliability. After removing these irrelevant fault features, the remaining trajectory, which represents the target fault feature, is marked by a green dashed box as the target region.

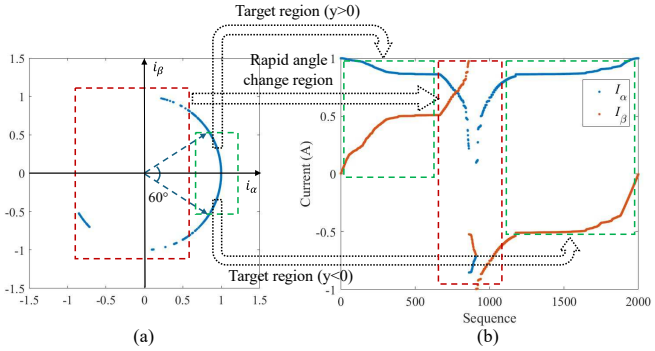

Fig. 3. Current vector trajectory passes through the positive x-axis, PMSM work at 500r/min, 1.5Nm, T35 OC. (a) Current vector trajectory, rapid angle change region crosses the positive x-axis. (b) Sorted normalized current vector.

Fig. 2(d) presents the sorted normalized currents vector i_{sncv} waveform, revealing that if the current space vector trajectory obtained in Step 2 does not cross the positive x-axis, the rapid angle change region will be clustered on both sides of the waveform. On the other hand, Fig. 3 illustrates another scenario where the current space vector trajectory crosses the positive x-axis, and it can be observed that the rapid angle change region is clustered at a middle position of the waveform after current sorting.

To demonstrate all 22 target fault features extracted by the proposed method, Fig. 4 presents the sorted normalized current vector sequence when all switches are healthy. Fig. 5 and Fig. 6 depict the normalized current vector sequences for scenarios where one switch and two switches experience an OC fault, respectively. In these figures, the red line represents i_α and the blue line represents i_β.

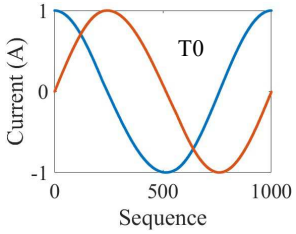

Fig. 4. Sorted normalized current vector sequence in a healthy state (blue line: i_α, red line: i_β).

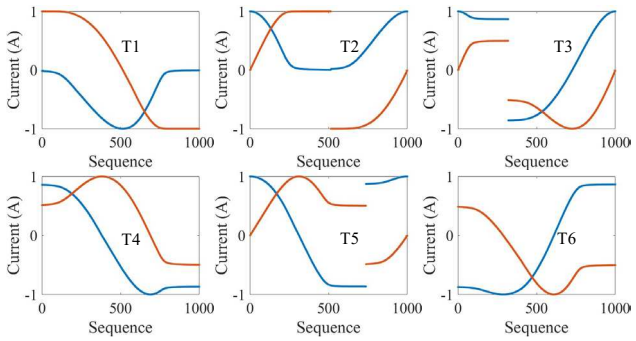

Fig. 5. Sorted normalized current vector sequence with a single switch OC fault (blue line: i_α, red line: i_β).

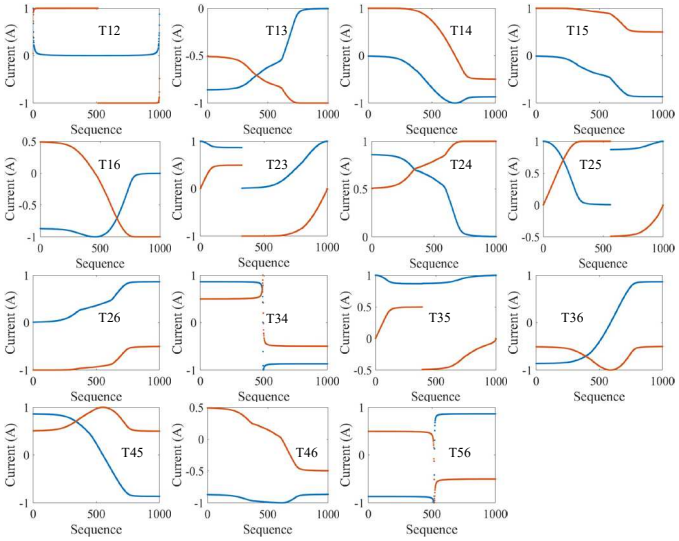

Fig. 6. Sorted normalized current vector sequence with two switches OC faults (blue line: i_α, red line: i_β).

III. Simulation Validation

This proposed fault diagnosis method follows a structured process, as illustrated in the block diagram in Fig. 7. First, three phase current i_{abc} data under various fault conditions is obtained through Simulink simulation. The i_{abc} signals are then transformed into fault pattern i_{sncv} using the feature extraction method described in Section II, after which the dataset is split into training and validation sets. A 1D-CNN is then employed to learn from the training data, while validation accuracy is used to assess the model performance. Once the optimal model is trained, it is applied to real motor fault diagnosis, where real motor operation data undergoes the same feature extraction process before being fed into the trained model for fault prediction.

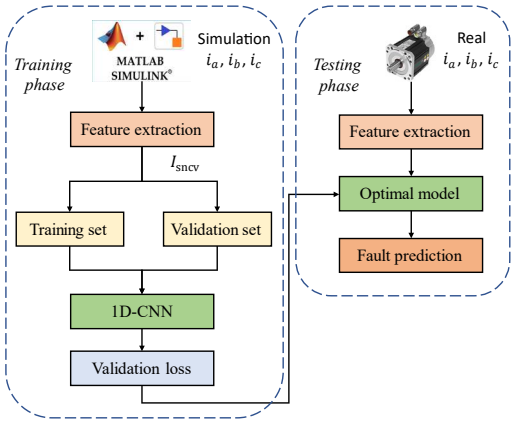

Fig. 7. Block diagram of the proposed fault diagnosis method.

A. 1D-CNN Architecture

A 2-channel 1D-CNN was designed to differentiate various types of inverter OC faults. As shown in Fig. 8, the input to the CNN is the sorted and normalized current sequence, with a size of 200×2 (sequence length × number of channels), as the high-frequency information is sorted to the rapid angle change regions, 200 data points is enough to describle the fault pattern and the computation budern is also elleviated. The architecture consists of two convolutional layers, followed by a ReLU activation function and a max pooling layer. Table II lists the layer-by-layer configuration of proposed 1D-CNN network, Both the first and second convolutional layers employ a kernel size of 3 and a stride of 1, extracting fine-grained local features and, through stacking, effectively expanding the receptive field to capture longer-range dependencies. The ReLU activation function introduces sparsity and accelerates convergence by activating only positive values. Max pooling downsamples by taking local maxima, reducing dimensions while preserving key features and improving positional invariance. After the second max pooling layers, global average pooling (GAP) is applied to reduce the spatial dimensions of the feature maps by averaging each feature map, effectively preserving global information while minimizing parameters to reduce the risk of overfitting. Following GAP, a flatten layer is added to transform the multi-dimensional feature maps into a one-dimensional vector, ensuring seamless integration and compatibility with the subsequent fully connected (FC) layer. The FC layer which consists of 22 neurons, corresponding to the number of fault classes, is then used for classification. The final fault diagnosis prediction is produced by a Softmax layer, which converts the output logits into a probability distribution over the fault classes. Each class is assigned a probability value between 0 and 1, ensuring the sum of probabilities equals 1, thus enabling clear and interpretable predictions. In addition, the sorting mechanism clusters irrelevant fault feature toward the sequence ends or middle, acting as a filtering step to some extent. The inherent translation invariance of the 1D-CNN architecture further enhances the model robustness by making it tolerant to the specific positions of features within the sequence. Notably, this simple 1D-CNN network comprises only 2406 learnable parameters and requires just 0.35 MFLOPs for a single forward

pass. We adopt a lightweight 1D-CNN because it matches the angle-sorted normalized-current representation and provides robustness against fault-pattern variations.; Section IV provides the empirical comparisons that verify this choice.

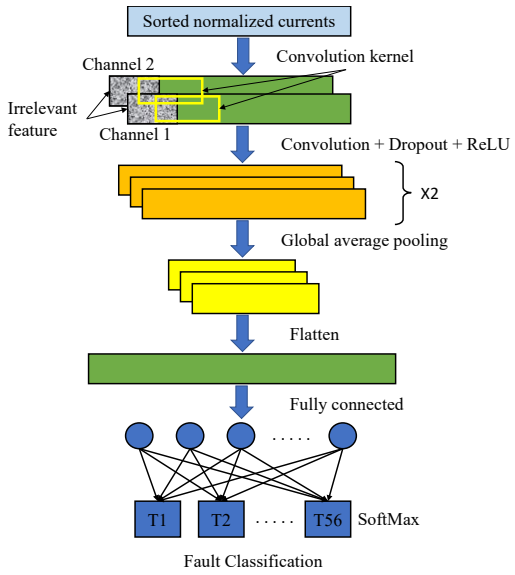

Fig. 8. Architecture of the proposed 1D-CNN for OC fault diagnosis.

TABLE II
LAYER-BY-LAYER CONFIGURATION OF PROPOSED 1D-CNN NETWORK

Layers	Input size	Output size	Kernel size/ stride	Activation function
Input layers	200×2	2×200	-	-
Convolution layer 1	2×200	16×200	3,1	ReLU
Pooling layer 1	16×200	16×100	2,2	-
Convolution layer 2	16×100	32×100	3,1	ReLU
Pooling layer 2	32×100	32×50	2,2	-
GAP layer	32×50	32×1	-	-
FC layer	32	22	-	-
Softmax layer	22	22	-	Softmax

B. Pretraining with Simulation Data

To improve the robustness of the fault diagnosis under various operating conditions, this paper simulated the current characteristics of a 2.1kW PMSM, with specifications outlined in Table III. Simulations were performed at various speeds (600 r/min, 850 r/min, 1100 r/min, 1350 r/min, 1600 r/min, 1850 r/min, 2100 r/min, 2350 r/min, 2600 r/min) and loads (1 Nm, 1.3 Nm, 1.6 Nm, 1.9 Nm, 2.2 Nm, 2.5 Nm, 2.8 Nm, 3.1 Nm, 3.4 Nm, 3.7 Nm, 4Nm) under both healthy state and 21 OC fault states. This generated a training dataset comprising 2178 samples. The model was trained using the Adam optimizer with mini-batch training. The input data was structured into batches of size $m \times n \times l$, where the batch size m=32, the sequence length n=200, and the number of channels l=2.

TABLE III
PARAMETERS OF THE PMSM WITH OC FAULTS

Parameters	Unit	Value
Number of pole pairs	--	3
Rated speed	r/min	3000
Rated torque	N	6.7
Rated power	kW	2.1
Stator resistance	Ohm	2.25
d-axis inductance	mH	11
q- axis inductance	mH	17
Permanent magnet flux linkage	Wb	0.25

To determine the most suitable pretrained model, the simulation data was split into a training set and a validation set, with the validation accuracy used as the metric for hyperparameter tuning. To assess the accuracy of the proposed fault extraction method, the validation accuracy of a 1D-CNN against several baseline machine learning methods is compared, including k-nearest neighbor (KNN), support vector machine (SVM), random forest (RF), Bayesian network (BN), deep belief network (DBN), and long short-term memory (LSTM), as summarized in Table IV. The optimal hyperparameters for each method were identified through grid search. As presented in Table II, the proposed 1D-CNN, along with KNN, SVM, and RF, achieved 100% validation accuracy. Meanwhile, BN, DBN, and LSTM yielded accuracy levels of 99.63%, 99.77%, and 98.85%, respectively. Although all methods appear to fit the validation set well, these results alone do not definitively indicate the most suitable model, as they may be overfitting the simulation data. Therefore, to rigorously evaluate each model's generalization performance, these pre-trained models will be tested on more challenging real-world datasets, as shown in Section IV.

TABLE IV
SIMULATION COMPARISON OF ACCURACY OF METHODS

Models	1D CNN	KNN	SVM	RF	BN	DBN	LSTM
Validation accuracy (%)	100	100	100	100	99.6	99.8	98.9

IV. EXPERIMENT VALIDATION

The experimental validation of the proposed diagnostic strategy is conducted on the hardware setup shown in Fig. 9. The dynamometer consists of two Nidec PMSM servo motors coupled through a shaft, with Plexim Rt-box 1 serving as a closed-loop controller for the test motor, three current probes for current sampling, and a Nidec inverter to drive the load motor. The proposed fault diagnosis method employs pre-trained 1D-CNN and several baseline models, which has been trained using simulation data from Section III. The OC fault for a given IGBT is represented by cutting off its control signal.

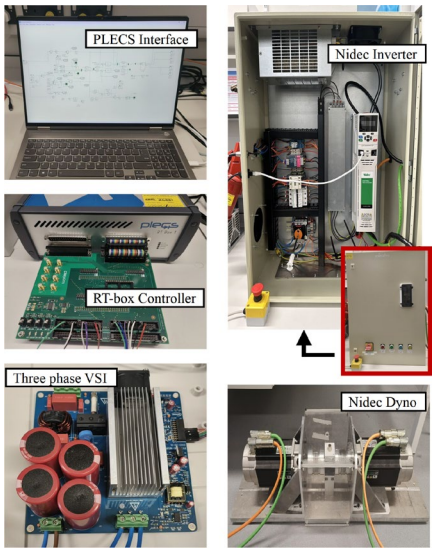

Fig. 9. Experiment setup.

A. Offline Accuracy Test

To validate the accuracy of the proposed model, an offline accuracy test was initially conducted under various operating conditions. The experimental scenarios included three rotational speeds (600 r/min, 1200 r/min and 1800 r/min) and three different load torques (2 Nm, 3 Nm and 4Nm), as detailed in Table V. For 2 Nm and 3 Nm load torque operations, the tests covered all 22 fault types. However, at a torque of 4 Nm, testing was limited to a single switch OC scenario due to safety concerns. Subsequently, three-phase current data over one electrical cycle were collected, resulting in a test set comprising 153 samples.

TABLE V
OPERATING CONDITIONS OF THE PMSM IN EXPERIMENTS

Rotation speed	Load torque	Fault class
600r/min	2Nm	All 22 types of OC
	3Nm	All 22 types of OC
	4Nm	One switch OC
1200r/min	2Nm	All 22 types of OC
	3Nm	All 22 types of OC
	4Nm	One switch OC
1500r/min	2Nm	All 22 types of OC
	3Nm	All 22 types of OC
	4Nm	One switch OC

In this study, the pre-trained models were directly deployed on the experimental data, without fine tuning, to straightforwardly assess each model's capability to generalize from simulation to real-world conditions. As shown in Table IV (Section III) and the no noise column of Table VI, most models exhibit decreased accuracy when transitioning from simulation to experimental data. Nevertheless, SVM achieves a good accuracy of approximately 98.85%, and 1D-CNN consistently maintains the highest classification rate at 100%. By contrast, KNN, RF and DBN experience moderate accuracy drops (dropping from 100%, 100% and 99.8% to 96.55%, 93.87% and 93.08%, respectively), whereas BN and LSTM show more pronounced declines (dropping from 99.6% and 98.9 % to 68.54% and 75.26%, respectively). These findings highlight the superior cross-domain generalization of the 1D-CNN-based approach.

TABLE VI
ACUURACY OF MODELS IN NOISELESS AMD NOISE ENVIRONMENT, UNIT: %

Methods	No noise	20dB	10dB
KNN	96.55	82.33	63.52
SVM	98.25	84.90	60.76
RF	93.87	82.38	60.80
BN	68.54	35.34	23.46
DBN	93.08	80.76	63.48
LSTM	75.26	52.10	32.6
1D-CNN	100	94.45	92.81

B. Robustness Validation

To further validate the robustness of the proposed fault diagnosis method, Gaussian white noise was added to the measured stator currents at signal-to-noise ratios (SNR) of 20 dB and 10 dB. The SNR is defined as

$$SNR = 10log_{10}\left(\frac{P_{signal}}{P_{noise}}\right),$$

where P_{signal} and P_{noise} are the power of signal and noise, respectively.

Fig. 10 demonstrates the impact of different noise conditions on the proposed fault pattern extraction method, showing the three-phase current waveforms i_{abc} and their sorted normalized current vectors i_{sncv} for SNRs of 0 dB, 20 dB, and 10 dB (Fig. 10(a), (c), (e) for i_{abc} and Fig. 10(b), (d), (f) for i_{sncv}). The presence of substantial additive noise severely distorts the measured current waveforms. Although i_{sncv} is also distorted, it retains relatively clear and distinguishable fault patterns compared to i_{abc}. The quantitative classification results in Table VI confirm this observation: as the SNR decreases, the accuracy of all methods decreases to various degrees, among which the accuracy of KNN, SVM and RF decreases significantly with the decrease of SNR (from 96.55%, 98.25% and 93.87% at no noise to 63.52%, 60.76% and 60.8% at 10 dB, respectively), BN and LSTM even falls below 40% at 10 dB, the proposed 1D-CNN maintains notably higher accuracy (only decreasing from 100% at no noise to 92.81% at 10 dB). Compared with the baseline models, the 1D-CNN achieves superior low-SNR robustness by hierarchically applying local convolutional filters and pooling to emphasize salient features and suppress noise.

C. Data Augmentation

By analyzing the current signals i_{abc} and their corresponding fault features i_{sncv} under different SNR conditions (as shown in Fig. 10), it can be observed that when Gaussian noise is added to the three-phase current signals and then mapped through the proposed fault feature extraction method, the resulting features are not merely a simple superposition of

Gaussian noise. If the feature extraction process is represented as a nonlinear function $f(x)$, and the Gaussian noise is denoted as a constant ϵ, then the noisy three-phase currents can be expressed as $x + \epsilon$. Due to the inherent nonlinearity of $f(\cdot)$, the transformation of $x + \epsilon$ in the feature space is not simply equivalent to $f(x) + f(\epsilon)$, but rather introduces unpredictable perturbations.

Compared to directly adding noise to the extracted features, injecting noise at the raw signal level before performing nonlinear feature extraction leads to a more diverse sample distribution. Based on this principle, data augmentation was implemented during the training phase: Gaussian noise of varying intensities was randomly added to the simulated three-phase currents before applying the fault feature extraction process. Table VII indicates that, compared with the benchmark model without augmentation, the model trained with noise augmentation maintains 100% accuracy on the noise-free test set. Under 20 dB and 10 dB SNR test conditions, the accuracies reach 97.82% and 94.77%, respectively, which show improvements of 3.37% and 1.96% with respect to the model without data augmentation. These results confirm that noise augmentation enhances the model robustness against noisy operating conditions.

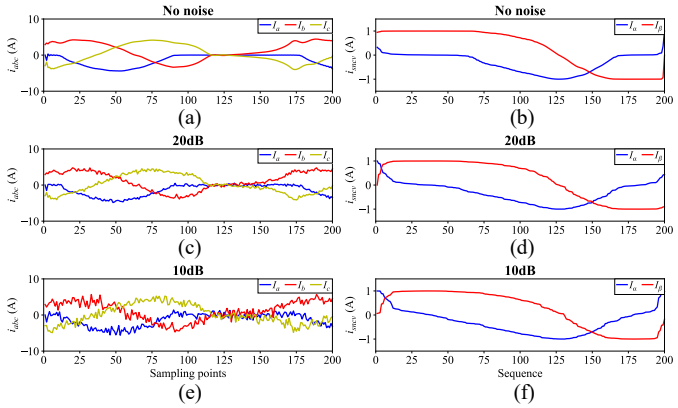

Fig. 10. Three phase currents and sorted normalized current vectors at 1200 r/min and 2Nm, T1 fault. (a) i_{abc} without noise. (b) i_{sncv} without noise. (c) 20dB i_{abc}. (d) 20dB i_{sncv}. (e) 10dB i_{abc}. (f) 10dB i_{sncv}.

TABLE VII
IMPACT OF DATA AUGMENTATION ON 1DCNN PERFORMANCE, UNIT: %

noise level	without data augmentation	with data augmentation	changes
no noise	100	100	0
20dB	94.45	97.82	+3.37
10dB	92.81	94.77	+1.96

D. Robustness under Dynamic Operation and Motor-Parameter Shift

To validate the robustness of the proposed fault diagnosis method under varying conditions. We first evaluated dynamic operation using experiment records where an OC fault was present while the drive underwent (a) a load change from 2 to 4 Nm at 1000 r/min and (b) a speed change from 1000 to 1500 r/min at 4 Nm (both T2 OC). As shown in Fig. 11(a), the three-phase current i_{abc} exhibits amplitude gradation after the load increases (the current amplitude rises sharply), whereas in Fig. 11(b) the speed change induces time warping in i_{abc}, the electrical period shortens (the waveform appears narrower) with amplitude slightly increased. In Fig. 11, the operating condition changes at time = 0.2 s, for one-electrical-cycle windows taken during and after the changes, the sorted normalized current features remain similar with steady-state patterns, and the pretrained 1D-CNN predicted the same fault class.

In addition, to assess robustness against simulation-to-reality parameter drift, a single-step parameter shift test (e.g., R_s, ψ_f, L_d, L_q) at 3000 r/min, 3 Nm, T45 OC is performed. The feature is computed from amplitude-normalized current space vectors followed by angle-based sorting, which largely removes uniform current scaling and limits the impact of moderate waveform deformations on the ordered angular shape. Using a nominally trained model, the nominal versus perturbed fault patterns under four representative composite settings were compared: (a) $1.2\ L_d$, $1.2\ L_q$, $1.2\ R_s$, $1.05\ \psi_f$; (b) $0.8L_d, 0.8L_q, 0.8R_s, 0.9\psi_f$; (c) $1.2L_d, 0.8L_q, 1.2R_s, 0.9\psi_f$; (d) $0.8\ L_d$, $1.2\ L_q$, $0.8\ R_s$, $1.05\ \psi_f$. As depicted in Fig. 12, the perturbed versus nominal sorted normalized current vector i_{sncv} show high similarity, and classifier-level evaluation with the pretrained 1D-CNN indicates unchanged predicted classes, suggesting insensitivity to realistic parameter mismatch.

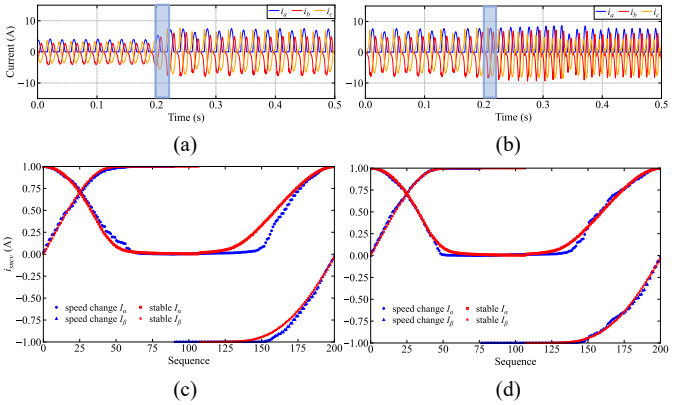

Fig. 11. Comparison of dynamic state and steady state. (a) i_{abc} with load changes. (b) i_{abc} with speed changes. (c) i_{sncv} with load changes. (d) i_{sncv} with speed changes.

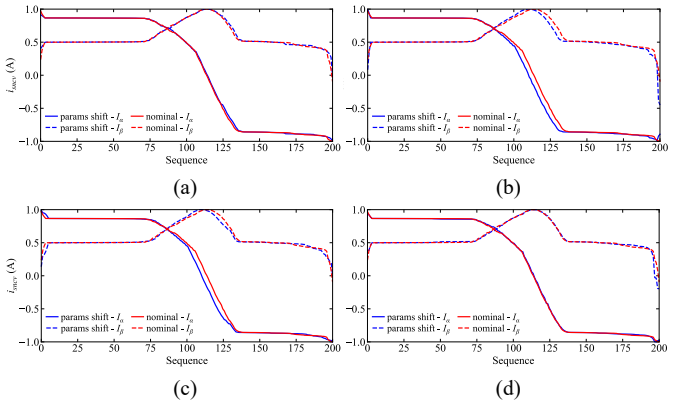

Fig. 12. Comparison of the perturbed i_{sncv} vs nominal i_{sncv}. (a) $1.2L_d$, $1.2L_q$, $1.2R_s$, $1.05\psi_f$. (b) $0.8L_d$, $0.8L_q$, $0.8R_s$, $0.9\psi_f$. (c) $1.2L_d$, $0.8L_q$, $1.2R_s$, $0.9\psi_f$. (d) $0.8L_d$, $1.2L_q$, $0.8R_s$, $1.05\psi_f$

E. Online Fault Diagnosis

To further validate the practicality of the proposed method, an online real-time diagnosis test was performed. The fault diagnosis model was trained on a Windows platform using PyTorch, and subsequently converted into the ONNX (Open Neural Network Exchange) format to leverage its superior cross-platform compatibility and faster inference speeds. The ONNX-based model was then deployed on a Raspberry Pi 5 for real-time diagnosis tasks. A Raspberry Pi Pico 2, equipped with an integrated ADC, was utilized to digitize the motor current signals, and transmit them to Raspberry Pi 5 using a sliding-window approach. The current sampling frequency was set to 10 kHz, and each sampling window captured data over one electrical cycle T, consisting of 200 points in each window and total 200×3 points for three phase currents. The sliding stride $\triangle$ was set to $T/10$ to ensure faster diagnosis.

In data-driven fault diagnosis schemes, the total diagnosis time is composed of the data preprocessing time, the inference time, and the communication time. Here, inference time is defined as the interval between 1D-CNN receiving fault-relevant features and outputting the classification result. Prior to inference, data preprocessing is conducted, which includes Clarke transformation, amplitude normalization, and data sorting. The communication delay is relatively small compared to the sampling window. By monitoring the Raspberry Pi's command log, the average data preprocessing time and inference time were found to be 0.22 ms and 0.20 ms, respectively —both significantly shorter than the sliding stride, ensuring real-time diagnosis.

The online fault diagnosis test was conducted on five different OC fault types: (a) single switch T3 OC; (b) one-phase double switch T12 OC, (c) upper bridge leg double switch T15 OC; (d) lower bridge leg double switch T24 OC; and (e) upper and lower bridge leg double switch T16 OC.

In Fig. 13(a), at time = 0.08 s, the T3 IGBT gate signal is disabled, causing a significant distortion in the three-phase current waveforms. The blue transparent box highlights the first electrical cycle immediately following the fault occurrence, where the fault indicator (FI) signal confirms a successful diagnosis in less than one electrical period. In Fig.13(b), at time = 0.08 s, T1 and T2 are disabled simultaneously (T12), the fault indicator undergoes a step change shortly after the fault, and a brief misdiagnosis appears immediately after the event. This arises from mixed windows that straddle the change point and is inherent to fixed-length, window-based labeling. With a one-cycle window of length T and stride $\triangle = T/10$, the worst-case time to stable localization is approximately $T + \triangle$ (the first fully post-fault window), while typical stabilization is close to T. The chosen stride $T/10$ balances update rate and stability and matches our measurements, where most faults are localized within about one electrical cycle. In Fig. 13(b), the T12 OC is stably identified after slightly more than one electrical cycle (about 1.1 cycles).

Fig. 13(c), (d) and (e) depict double-switch OC simulated by sequentially disabling two switches. In all other cases, the fault is successfully identified within one electrical cycle. Notably, in Fig. 13(c) (T15 OC, T5 then T1 disabled sequentially), a brief misdiagnosis occurs immediately after T5 opens, but the method accurately localizes the fault within approximately one electrical cycle. In the majority of cases, this first decision already identifies the correct switch. When the first window after the fault mixes healthy and faulty samples, the angle-sorted pattern departs from the healthy manifold, and the 1D-CNN can exploit these partial but discriminative cues to flag the fault early.

The online pipeline uses a one-electrical-cycle window (200 samples at 10 kHz) with a stride of $T/10$. Measured preprocessing and inference times on Raspberry Pi 5 (ONNX Runtime) are 0.22 ms and 0.20 ms, both well below the stride, so latency is dominated by the window length. The sorted, amplitude-normalized feature benefits from approximately one electrical period to form a stable discriminative pattern, and a lightweight 1D-CNN ($\approx$2406 parameters, $\approx$0.35 MFLOPs) effectively leverages this representation to diagnose 21 OC types with strong robustness and without experimental training data.

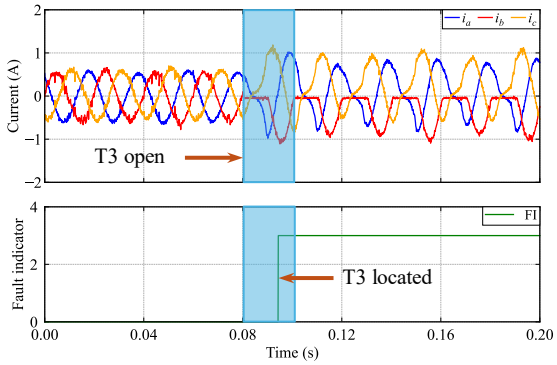

(a)

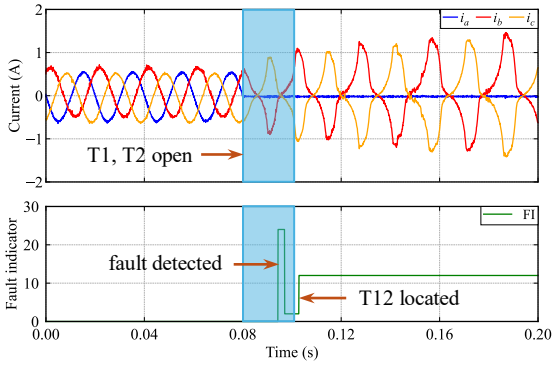

(b)

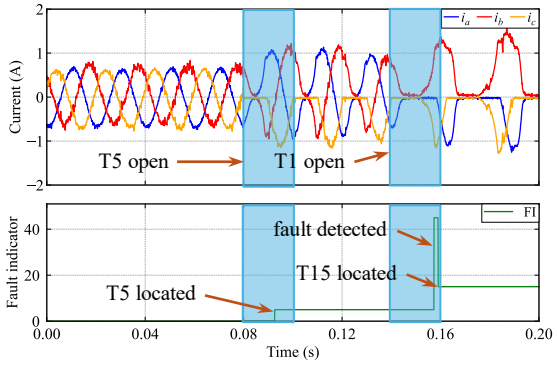

(c)

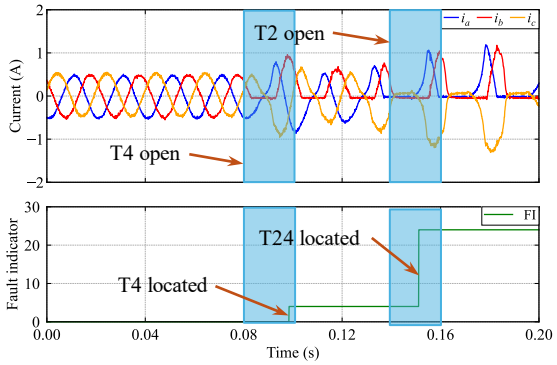

(d)

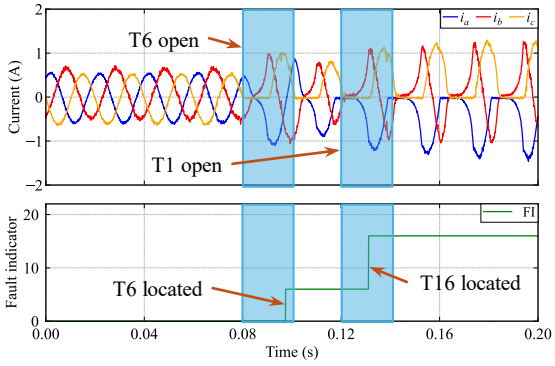

(e)

Fig. 13. Real time fault diagnosis results. (a) T3 OC. (b) T12 OC. (c) T15 OC. (d) T24 OC. (e) T16 OC.

F. Comparison with Other Methods

To further validate the effectiveness and competitiveness of the proposed diagnostic methodology, this section presents a comparative analysis with several state-of-the-art open-circuit fault diagnosis methods for three-phase inverters. Table VIII, which summarizes findings from prior studies, highlights key performance indicators, including signal type, load and speed invariance, parameter sensitivity, computational complexity, fault coverage, diagnosis time, and accuracy. For a fair comparison across AI methods, Table VIII also reports

TABLE VIII
COMPARISON WITH OTHER METHODS

Method	Signal type	Load invariant	Speed invariant	Parameter sensitivity	Computational burden (MFLOPs, Params)	OCF types	Diagnosis time	Accuracy
Proposed method	3-phase currents	Yes	Yes	Low	Low (0.35, 2406)	21	About 1 cycle	100
Wavelet CNN + normalized current vector trajectory [28]	3-phase currents	Yes	Yes	Low	High (6.83, 846806)	21	/	100
Seasonal–Trend decomposition [10]	3-phase currents	Yes	Yes	Low	Low	9	1.1-1.3 cycles	100
Manifold feature learning + ELM [20]	3-phase currents	Yes	Yes	Low	Medium	21	>1 cycle	96.76
RF + current trajectory slope [18]	3-phase currents	Yes	No	Low	Medium	6	About 1 cycle	>97
DFT + PCA [11]	3-phase currents	Yes	No	Low	Medium	21	<1/4 cycle	/
MPC+ currents signature [7]	3-phase currents	Yes	Yes	Medium	Medium	21	<1 cycle	<100
Multisource information fusion+1DCNN [29]	3-phase currents and 3-line voltages	Yes	Yes	Low	Medium (1.03, 5179)	21	/	100
Three rotatory reference systems + arithmetic operations [13]	3-phase currents and line currents	Yes	No	Low	Low	21	1/2 cycle	<100
DNN [22]	3-phase currents	No	Yes	Low	High (1.44, 722322)	21	/	97.97-99.23
Luenberger observer + current residuals analysis [5]	3-phase currents	Yes	Yes	Medium	Low	15	<1/4 cycle	100

* FLOPs are computed for a single-sample forward pass based on layer specifications reported in each paper; batch effects and data pre-processing are excluded for cross-paper consistency.
* For WCNN, the unit count of F_9 is not specified; we adopt 128 as a conservative setting. Using a range of 64–256 yields the same order of magnitude and does not change conclusions.

MFLOPs per forward pass and parameter counts, calculated from each model's layer specification. Our model requires 0.35 MFLOPs and 2,406 parameters, substantially lower than the three AI baselines.

As demonstrated in Table VIII, while many existing approaches achieve load and speed invariance [28], [20], [29], this often comes with the cost of higher complexity, extensive training data requirements, or both. For instance, the models in [28] and [20] require large experimental datasets and complex network architectures to ensure robustness. In contrast, the proposed method in this paper retains load and speed invariance with minimal parameter sensitivity and lower structural complexity. Another key advantage of the proposed approach is the reliance on simulation data rather than large-scale experimental datasets. Approaches in [20], [18], [22] often require tens of thousands of experimental samples, increasing both time and cost. By contrast, the proposed simulation-based strategy simplifies dataset acquisition while maintaining high diagnostic accuracy. In terms of fault coverage, the proposed method can diagnose 21 open-circuit faults, surpassing [10], [18], [5], ensuring broader applicability across different inverter systems. Regarding diagnosis speed, our method identifies OC faults with approximately one electrical cycle. While some existing signal or model based methods [11], [13], [5] report sub-cycle speeds (<1/4 cycle), they typically rely on stricter modeling assumptions and have a more limited applicability across operating conditions and inverter configurations. Our near-cycle detection reflects a deliberate design choice to prioritize feature stability and robustness with low computational cost, broad fault coverage, and the significant advantage of not requiring experimental training data, offering a practical balance for industrial deployment.

Overall, the proposed approach provides accurate, comprehensive, and robust diagnosis with reduced training demands and network complexity, making it a practical and efficient solution compared to existing methods.

V. Conclusion

The proposed fault feature extraction method processes the three-phase currents of the PMSM when the inverter OC fault happens. It transforms these currents into two-phase αβ axes currents using Clarke transform, normalizes their amplitudes, and then sorts the resulting current vectors in ascending order based on their 2-argument arctangent values. This approach ensures that the extracted fault features remain robust across various speeds and load conditions of the PMSM. To reduce fault data acquisition costs, the training dataset is generated by simulating the PMSM open-circuit fault model in Simulink, eliminating the need for extensive real-world fault data collection. For fault classification, this paper proposes a lightweight 1D-CNN with two convolutional layers, capable of diagnosing 21 OC states. The robustness of the model is further enhanced through data augmentation applied during pretraining. The effectiveness of the proposed data-driven fault diagnosis method was validated through simulations, offline experiments, and real-time hardware-in-the-loop (HIL) tests. It should be noted that with only two current sensors, sensor faults may be indistinguishable from single-leg OCs, whereas in our three-sensor setup they can be separated by current-balance checks. Compared to existing methods, the proposed approach demonstrates superior robustness, accuracy, and computational efficiency, making it a practical and efficient solution for real-world inverter fault diagnosis.

References

[1] W. Li, H. Li, X. Chen, A. Griffo, and X. Sun, "A Novel 1D-CNN Open Circuit Fault Diagnosis for PMSM Drives Using Normalized Current Space Vector Sorting," in *2024 IEEE Energy Conversion Congress and Exposition (ECCE)*, Phoenix, AZ, USA: IEEE, Oct. 2024, pp. 6478–6483. doi: 10.1109/ECCE55643.2024.10860788.

[2] Bin Lu and S. K. Sharma, "A Literature Review of IGBT Fault Diagnostic and Protection Methods for Power Inverters," *IEEE Trans. on Ind. Applicat.*, vol. 45, no. 5, pp. 1770–1777, 2009, doi: 10.1109/TIA.2009.2027535.

[3] M. Alavi, Danwei Wang, and Ming Luo, "Short-Circuit Fault Diagnosis for Three-Phase Inverters Based on Voltage-Space Patterns," *IEEE Trans. Ind. Electron.*, vol. 61, no. 10, pp. 5558–5569, Oct. 2014, doi: 10.1109/TIE.2013.2297298.

[4] S.-M. Jung, J.-S. Park, H.-W. Kim, K.-Y. Cho, and M.-J. Youn, "An MRAS-Based Diagnosis of Open-Circuit Fault in PWM Voltage-Source Inverters for PM Synchronous Motor Drive Systems," *IEEE Trans. Power Electron.*, vol. 28, no. 5, pp. 2514–2526, May 2013, doi: 10.1109/TPEL.2012.2212916.

[5] I. Jlassi, J. O. Estima, S. K. El Khil, N. M. Bellaaj, and A. J. M. Cardoso, "A Robust Observer-Based Method for IGBTs and Current Sensors Fault Diagnosis in Voltage-Source Inverters of PMSM Drives," *IEEE Trans. on Ind. Applicat.*, vol. 53, no. 3, pp. 2894–2905, May 2017, doi: 10.1109/TIA.2016.2616398.

[6] C. Shu, C. Ya-Ting, Y. Tian-Jian, and W. Xun, "A Novel Diagnostic Technique for Open-Circuited Faults of Inverters Based on Output Line-to-Line Voltage Model," *IEEE Trans. Ind. Electron.*, vol. 63, no. 7, pp. 4412–4421, Jul. 2016, doi: 10.1109/TIE.2016.2535960.

[7] W. Huang *et al.*, "Current-Based Open-Circuit Fault Diagnosis for PMSM Drives With Model Predictive Control," *IEEE Trans. Power Electron.*, vol. 36, no. 9, pp. 10695–10704, Sep. 2021, doi: 10.1109/TPEL.2021.3061448.

[8] Q.-T. An, L. Sun, and L.-Z. Sun, "Current Residual Vector-Based Open-Switch Fault Diagnosis of Inverters in PMSM Drive Systems," *IEEE Trans. Power Electron.*, vol. 30, no. 5, pp. 2814–2827, May 2015, doi: 10.1109/TPEL.2014.2360834.

[9] Q.-T. An, L.-Z. Sun, K. Zhao, and L. Sun, "Switching Function Model-Based Fast-Diagnostic Method of Open-Switch Faults in Inverters Without Sensors," *IEEE Trans. Power Electron.*, vol. 26, no. 1, pp. 119–126, Jan. 2011, doi: 10.1109/TPEL.2010.2052472.

[10] Y. Zhou, J. Zhao, Y. Song, J. Sun, H. Fu, and M. Chu, "A Seasonal–Trend-Decomposition-Based Voltage-Source-Inverter Open-Circuit Fault Diagnosis Method," *IEEE Trans. Power Electron.*, vol. 37, no. 12, pp. 15517–15527, Dec. 2022, doi: 10.1109/TPEL.2022.3190937.

[11] X. Sun, C. Song, Y. Zhang, X. Sha, and N. Diao, "An Open-Circuit Fault Diagnosis Algorithm Based on Signal Normalization Preprocessing for Motor Drive Inverter," *IEEE Trans. Instrum. Meas.*, vol. 72, pp. 1–12, 2023, doi: 10.1109/TIM.2023.3268461.

[12] R. B. Dhumale and S. D. Lokhande, "Neural Network Fault Diagnosis of Voltage Source Inverter under variable load conditions at different frequencies," *Measurement*, vol. 91, pp. 565–575, Sep. 2016, doi: 10.1016/j.measurement.2016.04.051.

[13] J. A. Reyes-Malanche, F. J. Villalobos-Pina, E. Cabal-Yepez, R. Alvarez-Salas, and C. Rodriguez-Donate, "Open-Circuit Fault Diagnosis in Power Inverters Through Currents Analysis in Time Domain," *IEEE Trans. Instrum. Meas.*, vol. 70, pp. 1–12, 2021, doi: 10.1109/TIM.2021.3082325.

[14] W. Wang, Y. Mao, P. Cui, J. Fu, W. Hua, and M. Cheng, "Double Normalization Fault Diagnosis Method for Open-Circuit Faults of PMSM Drives," *IEEE Trans. Power Electron.*, vol. 39, no. 9, pp. 11613–11624, Sep. 2024, doi: 10.1109/TPEL.2024.3404402.

[15] Y. Teng, X. Guo, Y. Wei, J. Zhao, and P. Zhang, "A Novel Short-Circuit Fault Diagnosis Method for Three-Phase Current Source Converter,"

IEEE Trans. Power Electron., vol. 39, no. 12, pp. 16792–16802, Dec. 2024, doi: 10.1109/TPEL.2024.3444737.

[16] S. Rokocakau *et al.*, "Fault Diagnosis Using Shallow Neural Networks for Voltage Source Inverters in Motor Drives," *IEEE Trans. on Ind. Applicat.*, vol. 60, no. 5, pp. 7038–7047, Sep. 2024, doi: 10.1109/TIA.2024.3409513.

[17] B. Cai, Y. Zhao, H. Liu, and M. Xie, "A Data-Driven Fault Diagnosis Methodology in Three-Phase Inverters for PMSM Drive Systems," *IEEE Trans. Power Electron.*, vol. 32, no. 7, pp. 5590–5600, Jul. 2017, doi: 10.1109/TPEL.2016.2608842.

[18] W.-C. Wang, L. Kou, Q.-D. Yuan, J.-N. Zhou, C. Liu, and G.-W. Cai, "An Intelligent Fault Diagnosis Method for Open-Circuit Faults in Power-Electronics Energy Conversion System," *IEEE Access*, vol. 8, pp. 221039–221050, 2020, doi: 10.1109/ACCESS.2020.3043796.

[19] F. Wu, K. Chen, G. Qiu, and W. Zhou, "Robust Open Circuit Fault Diagnosis Method for Converter Using Automatic Feature Extraction and Random Forests Considering Nonstationary Influence," *IEEE Trans. Ind. Electron.*, vol. 71, no. 10, pp. 13263–13273, Oct. 2024, doi: 10.1109/TIE.2023.3344816.

[20] Y. Xia and Y. Xu, "A Transferrable Data-Driven Method for IGBT Open-Circuit Fault Diagnosis in Three-Phase Inverters," *IEEE Trans. Power Electron.*, vol. 36, no. 12, pp. 13478–13488, Dec. 2021, doi: 10.1109/TPEL.2021.3088889.

[21] T. Shi, Y. He, T. Wang, and B. Li, "Open Switch Fault Diagnosis Method for PWM Voltage Source Rectifier Based on Deep Learning Approach," *IEEE Access*, vol. 7, pp. 66595–66608, 2019, doi: 10.1109/ACCESS.2019.2917311.

[22] H. Yan, Y. Peng, W. Shang, and D. Kong, "Open-circuit fault diagnosis in voltage source inverter for motor drive by using deep neural network," *Engineering Applications of Artificial Intelligence*, vol. 120, p. 105866, Apr. 2023, doi: 10.1016/j.engappai.2023.105866.

[23] L. Wen, X. Li, L. Gao, and Y. Zhang, "A New Convolutional Neural Network-Based Data-Driven Fault Diagnosis Method," *IEEE Trans. Ind. Electron.*, vol. 65, no. 7, pp. 5990–5998, Jul. 2018, doi: 10.1109/TIE.2017.2774777.

[24] S. Kiranyaz, A. Gastli, L. Ben-Brahim, N. Al-Emadi, and M. Gabbouj, "Real-Time Fault Detection and Identification for MMC Using 1-D Convolutional Neural Networks," *IEEE Trans. Ind. Electron.*, vol. 66, no. 11, pp. 8760–8771, Nov. 2019, doi: 10.1109/TIE.2018.2833045.

[25] S.-H. Kim, D.-Y. Yoo, S.-W. An, Y.-S. Park, J.-W. Lee, and K.-B. Lee, "Fault Detection Method Using a Convolution Neural Network for Hybrid Active Neutral-Point Clamped Inverters," *IEEE Access*, vol. 8, pp. 140632–140642, 2020, doi: 10.1109/ACCESS.2020.3011730.

[26] W. Yuan, Z. Li, Y. He, R. Cheng, L. Lu, and Y. Ruan, "Open-Circuit Fault Diagnosis of NPC Inverter Based on Improved 1-D CNN Network," *IEEE Trans. Instrum. Meas.*, vol. 71, pp. 1–11, 2022, doi: 10.1109/TIM.2022.3166166.

[27] C. Yao *et al.*, "Online Open-Circuit Fault Diagnosis for ANPC Inverters Using Edge-Based Lightweight 2D-CNN," *IEEE Trans. Power Electron.*, pp. 1–6, 2024, doi: 10.1109/TPEL.2024.3351911.

[28] J. Hang, X. Shu, S. Ding, and Y. Huang, "Robust Open-Circuit Fault Diagnosis for PMSM Drives Using Wavelet Convolutional Neural Network With Small Samples of Normalized Current Vector Trajectory Graph," *IEEE Trans. Ind. Electron.*, vol. 70, no. 8, pp. 7653–7663, Aug. 2023, doi: 10.1109/TIE.2022.3231304.

[29] J. Hang, G. Qiu, M. Hao, and S. Ding, "Improved Fault Diagnosis Method for Permanent Magnet Synchronous Machine System Based on Lightweight Multisource Information Data Layer Fusion," *IEEE Trans. Power Electron.*, vol. 39, no. 10, pp. 13808–13817, Oct. 2024, doi: 10.1109/TPEL.2024.3432163.